THE JOURNAL OF PHYSICAL CHEMISTRY Letters

pubs.acs.org/JPCL

Letter

Unraveling the Near-Unity Narrow-Band Green Emission in Zero-Dimensional Mn^{2+}-Based Metal Halides: A Case Study of $(C_{10}H_{16}N)_2Zn_{1-x}Mn_xBr_4$ Solid Solutions

Guojun Zhou,[¶] Zhiyang Liu,[¶] Jinglong Huang, Maxim S. Molokeev, Zewen Xiao,* Chonggeng Ma,* and Zhiguo Xia*

Cite This: *J. Phys. Chem. Lett.* 2020, 11, 5956−5962

Read Online

ABSTRACT: Zero-dimensional (0D) Mn^{2+}-based metal halides are potential candidates as narrow-band green emitters, and thus it is critical to provide a structural understanding of the photophysical process. Herein, we propose that a sufficiently long Mn−Mn distance in 0D metal halides enables all Mn^{2+} centers to emit spontaneously, thereby leading to near-unity photoluminescence quantum yield. Taking lead-free $(C_{10}H_{16}N)_2Zn_{1-x}Mn_xBr_4$ (x = 0−1) solid solution as an example, the Zn/Mn alloying inhibits the concentration quenching that is caused by the energy transfer of Mn^{2+}. $(C_{10}H_{16}N)_2MnBr_4$ exhibits highly thermal stable luminescence even up to 150 °C with a narrow-band green emission at 518 nm and a full width at half maximum of 46 nm. The fabricated white light-emitting diode device shows a high luminous efficacy of 120 lm/W and a wide color gamut of 104% National Television System Committee standard, suggesting its potential for liquid crystal displays backlighting. These results provide a guidance for designing new narrow-band green emitters in Mn^{2+}-based metal halides.

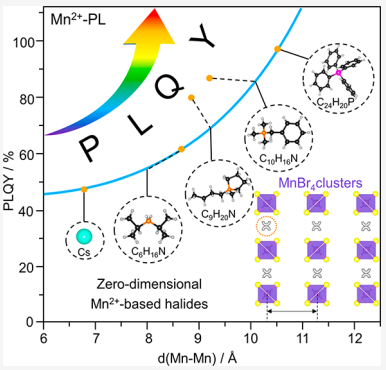

Design principle toward new photoluminescence (PL) materials used in light-emitting diodes (LEDs) backlights for liquid crystal displays (LCDs) is attractive, and a key factor determining the LCDs' color gamut is the full width at half-maximum (fwhm) of green and red emitters used in LEDs backlights.[1−3] Since human eyes can clearly distinguish green light, it is crucial to design superior green-light emitters with appropriate peak position, high photoluminescence quantum yield (PLQY), and excellent thermal stability to meet the need for industrial application. To date, there are three main categories of green emitters: semiconductor quantum dots (QDs), rare-earth-doped phosphors, and Mn^{2+}-activated phosphors. The green-emitting QDs mainly include II−VI QDs and perovskite QDs, represented by CdSe and $CsPbBr_3$, respectively, for which the applications are hindered by the toxicity of Cd and Pb and the relatively poor stability of perovskites.[4−6] As typical rare-earth phosphors, the narrow-band green-emitting β-Sialon:Eu^{2+} and $RbLi(Li_3SiO_4)_2$:Eu^{2+} (RLSOE) have received a great deal of attentions.[7−9] However, the relatively large fwhm (~55 nm) of β-Sialon:Eu^{2+} and limited stability of RLSOE deserves continued research efforts. For Mn^{2+}-activated phosphors, the absorption and emission behaviors of Mn^{2+} depend strongly on its coordination environment in the hosts. Octahedrally coordinated Mn^{2+} shows orange or red emission with a large fwhm (>60 nm),[10,11] whereas tetrahedrally coordinated Mn^{2+} exhibits green emission (500−550 nm) with a small fwhm of 25−60 nm.[12−14] $MgAl_2O_4$:Mn^{2+}, as a typical green emitter, exhibits a narrow emission peaked at 525 nm (fwhm = 35 nm), and its white LEDs show a wide color gamut of 116% National Television System Committee standard (NTSC). However, the d−d transitions of Mn^{2+} are parity-forbidden, leading to the relatively low PLQY and absorption efficiency as well as too long lifetime. Therefore, significant efforts have been devoted to the exploring superior narrow-band green emitters with high PLQY, relatively short lifetime, and excellent stability.

Recently, the discovery of luminescent zero-dimensional (0D) metal halides is attracting an increasing level of interest,[15,16] in which Mn^{2+}-based metal halides usually exhibit green or red emissions with high PLQY depending on the local structures, especially when the $[MnX_4]$ are surrounded by bulky organic ligands.[17−24] Kovalenko et al. found that the emission positions, fwhm, radiative lifetimes, and PLQYs depend strongly on the choice of halogen anions.[24] However, the crystal structure dependence of PL characteristics is still a challenge in 0D Mn^{2+}-based metal halides, which is critical to guide the further design of high-performance light-emitting

Received: June 23, 2020
Accepted: July 6, 2020
Published: July 6, 2020

https://dx.doi.org/10.1021/acs.jpclett.0c01933
J. Phys. Chem. Lett. 2020, 11, 5956−5962

materials. Herein, we studied the relationship between the Mn−Mn distance and luminescent efficiency in 0D Mn^{2+}-based metal halides and proposed a design principle toward the materials discovery with near-unity narrow-band green emission originated from Mn^{2+}. Specifically, a series of isostructural solid solutions $(C_{10}H_{16}N)_2Zn_{1-x}Mn_xBr_4$ (x = 0−1) have been designed and synthesized to unveil the isolated $[MnBr_4]$ unit functionalization for inhibiting concentration quenching caused by the energy transfer between the luminescence centers of Mn^{2+}. Results show that the solid solutions present a narrow-band green emission at 518 nm with a fwhm of 46 nm. The unique 0D isolated structure casts a much longer distance between any two adjacent Mn^{2+} ions, which enables all luminescence centers of Mn^{2+} with spontaneous emission. Besides, the thermal stability of solid solutions and the performances of white LED device have also been evaluated. This work is aimed at paving the way for a new understanding about the 0D Mn^{2+}-based metal halides toward the superior narrow-band phosphors for industrial application.

So far, we have synthesized Cs_3MnBr_5,[25] $(C_9H_{20}N)_2MnBr_4$,[22] and $(C_{10}H_{16}N)_2MnBr_4$ in our group, which shown bright narrow-band green emissions with PLQYs of 49%, 81.08%, and 88.75%, respectively. In addition, $(C_6H_{16}N)_2MnBr_4$ and $(C_{24}H_{20}P)_2MnBr_4$ with PLQYs of 62.2% and 98%, respectively, have also been reported.[19,21] As shown in Figure 1, we listed these Mn^{2+}-based metal halides

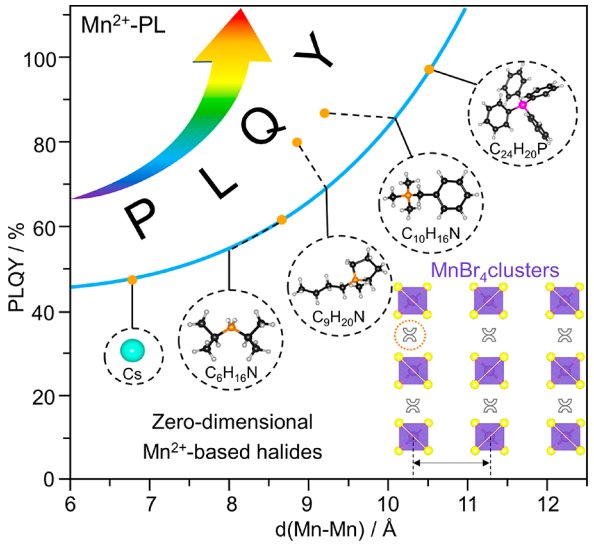

Figure 1. Illustration of the closest Mn−Mn distance and luminescent efficiency for the selected 0D Mn^{2+}-based metal halides. The crystal structure presents the isolated $[MnBr_4]$ units and the different ligands are embedded into pores of lattices to form Cs_3MnBr_5, $(C_6H_{16}N)_2MnBr_4$, $(C_9H_{20}N)_2MnBr_4$, $(C_{10}H_{16}N)_2MnBr_4$, and $(C_{24}H_{20}P)_2MnBr_4$. Their PLQYs show an increasing trend from 49% to 98%.

including Cs_3MnBr_5, $(C_6H_{16}N)_2MnBr_4$, $(C_9H_{20}N)_2MnBr_4$, $(C_{10}H_{16}N)_2MnBr_4$, and $(C_{24}H_{20}P)_2MnBr_4$, which have similar 0D structures with the $[MnBr_4]$ tetrahedrons isolated by the monovalent inorganic or organic cations. Note that the shape and the orientation of the $[MnBr_4]$ tetrahedrons can be affected by the monovalent cation spacers. Through a structural analysis, we find that the PLQYs of these compounds correlate strongly with their closest Mn−Mn distance (Table 1). The longer the distance between the adjacent Mn^{2+} ions,

Table 1. Photoluminescence Properties (Peak Position, PLQY) and Mn−Mn Distance in Various 0D Mn^{2+}-Based Metal Halides

chemical formula	peak position, nm	PLQY, %	Mn−Mn distance, Å	ref
Cs_3MnBr_5	520	49	6.793	25
$(C_6H_{16}N)_2MnBr_4$	525	62.2	8.854	19
$(C_9H_{20}N)_2MnBr_4$	528	81.08	8.952	22
$(C_{10}H_{16}N)_2MnBr_4$	518	88.75	9.179	this work
$(C_{24}H_{20}P)_2MnBr_4$	522	98	10.447	21

the higher the PLQY. We speculate that a sufficiently long Mn−Mn distance would enable all Mn^{2+} luminescence centers emit spontaneously, thereby achieving near-unity PL efficiency.

On that basis, we select $(C_{10}H_{16}N)_2MnBr_4$ as a typical case to reveal the relationship between the closest Mn−Mn distance and energy transfer rate with the increase of Mn^{2+} concentrations. Reassuringly, a series of isostructural solid solutions $(C_{10}H_{16}N)_2Zn_{1-x}Mn_xBr_4$ (x = 0−1) were designed and synthesized to unveil the isolated $[MnBr_4]$ unit functionalization for inhibiting concentration quenching caused by the energy transfer between the luminescence centers of Mn^{2+} under the only change of Mn^{2+} concentration. The experimental details are presented in the Supporting Information. The crystallographic data of $(C_{10}H_{16}N)_2Zn_{1-x}Mn_xBr_4$ (x = 0, 0.2, 0.4, 0.6, 0.8, 1) were obtained through Rietveld refinement, and their crystallographic information files (CIFs) are presented in the Supporting Information. Such refinements were stable with low R-factors (Table S1, Figure S1). All peaks were indexed by the same monoclinic cell ($P2_1$), and the site of Mn^{2+} ion was occupied by Mn/Zn ions with fixed occupancy according to the suggested chemical formula. The linear x dependences of the cell volumes (Figure 2a) and the average bond lengths $d(Mn/Zn-Br)_{average}$ (Figure 2b) further indicate that the Mn and Zn occupy the same crystallographic sites. Crystal

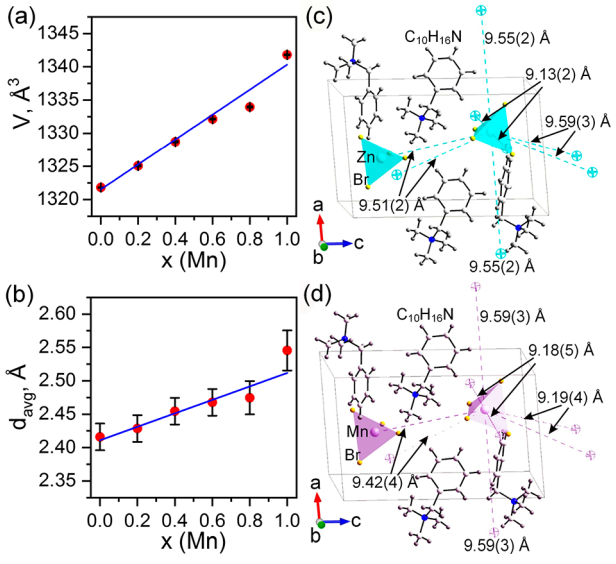

Figure 2. (a, b) Linear cell volume dependence $V(x)$ and average bond length $d(Mn/Zn-Br)_{average}$ of $(C_{10}H_{16}N)_2Mn_xZn_{1-x}Br_4$ (x = 0, 0.2, 04, 0.6, 0.8, 1). (c, d) Crystal structures of $(C_{10}H_{16}N)_2ZnBr_4$ and $(C_{10}H_{16}N)_2MnBr_4$ with the closest Zn−Zn and Mn−Mn distance.

https://dx.doi.org/10.1021/acs.jpclett.0c01933
J. Phys. Chem. Lett. 2020, 11, 5956−5962

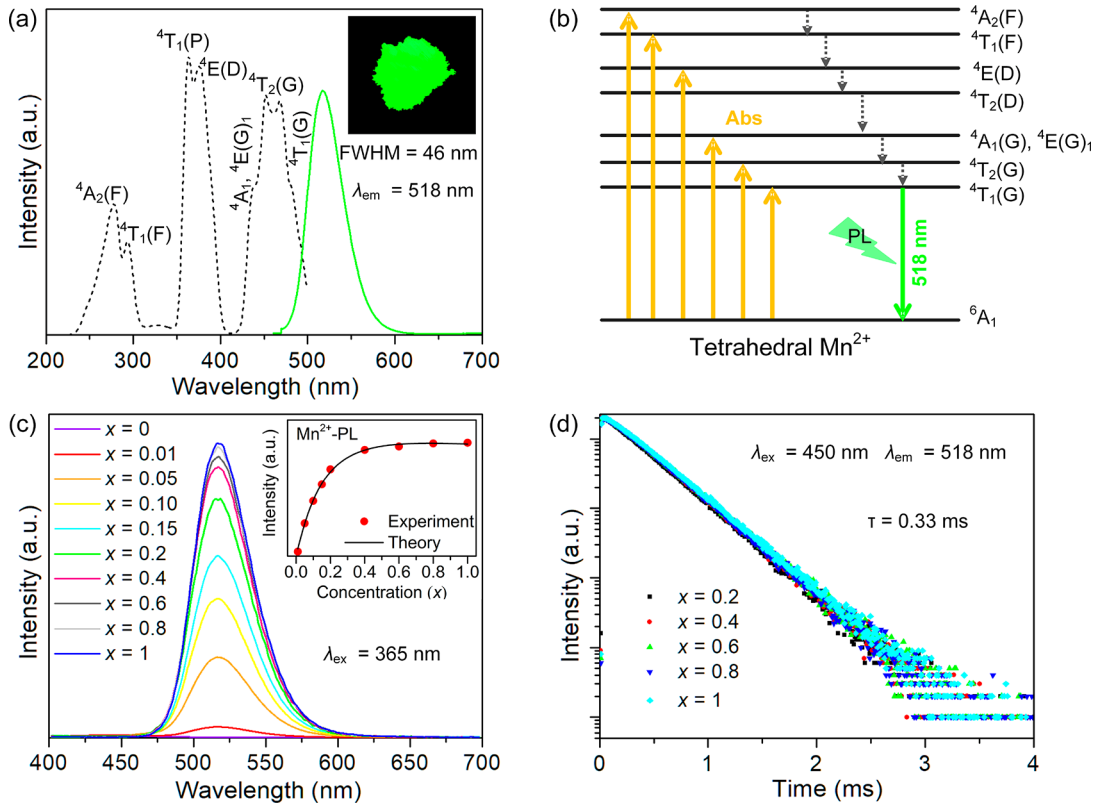

Figure 3. (a) PLE and PL spectra of $(C_{10}H_{16}N)_2MnBr_4$. The inset shows the digital photograph under 365 nm UV lamp. (b) Energy states splitting and optical transitions in tetrahedrally coordinated Mn^{2+}. (c) PL spectra of $(C_{10}H_{16}N)_2Zn_{1-x}Mn_xBr_4$ (x = 0−1) excited 365 nm under the same tested conditions. The inset is a variable trend of integrated intensity with the increase of Mn^{2+} concentration from experiment and theory, respectively. (d) Decay curves of $(C_{10}H_{16}N)_2Zn_{1-x}Mn_xBr_4$ (x = 0.2, 0.4, 0.6, 0.8, 1) under excitation at 450 nm, monitored at 518 nm.

structures with the closest Mn/Zn coordination spheres are shown in Figure 2c,d. The two end compounds are isostructural, with similarly distances between the closest tetrahedrons, i.e., 9.13 and 9.18 Å for Zn−Zn and Mn−Mn, respectively, in accordance with the trend of ion radii 0.60 and 0.66 Å for Zn^{2+} and Mn^{2+}, respectively.[26]

The PLE and PL spectra of the two end-member compounds are shown in Figure 3a and Figure S2a, respectively. $(C_{10}H_{16}N)_2ZnBr_4$ exhibits a blue emission (fwhm = 60 nm) peaked at 440 nm with a low PLQY less than 1% under 365 nm excitation. The Stokes shift of around 75 nm is small, different from the cases of self-trapped exciton emission.[27,28] Noted that the defect-induced emissions are common in Zn-based compounds.[29,30] Therefore, we speculate that the blue emission originates from vacancy defects. In addition, the weak blue emission has a lifetime of 152.64 ns (Figure S2b) and gradually disappears upon Mn^{2+} doping. As for the $(C_{10}H_{16}N)_2MnBr_4$, a narrow-band green emission (fwhm = 46 nm) at 518 nm under 450 nm excitation was observed (Figure 3a). The PLE spectrum shows three distinct groups of bands, with the corresponding electronic transitions summarized in Figure 3b. The narrow-band green emission is attributed to the d−d transition ($^4T_1$−$^6A_1$) of tetrahedrally coordinated Mn^{2+} centers.[23,24] The as-prepared powder shows an intense green light under 365 nm irradiation, as shown in the inset of Figure 3a.

The PL spectra of $(C_{10}H_{16}N)_2Zn_{1-x}Mn_xBr_4$($x$ = 0−1) are shown in Figure 3c. The inset of Figure 3c summarizes the Mn^{2+} concentration (x) dependence of the integrated intensities. As listed in Table 2, at the low x region, the PLQY increases with increasing the x, and reaches a plateau value of 89.06% at x = 0.4. Interestingly, the PLQY does not drop with further increasing the x, indicating these solid solutions are free of the common chemical quench effect. We speculate that the spontaneous emissions of Mn^{2+} competes with the nonradiation losses induced by the energy transfer of Mn^{2+}. The closest Mn−Mn distance is essential for the luminescence saturation behavior of Mn^{2+}. The large organic cations provide long Mn−Mn distance. Specifically, the unique arrangement of isolated [$MnBr_4$] units inhibit the migration of excitation energy in adjacent luminescence centers of Mn^{2+}, thereby leading to near-unity efficiency without interference of defects or other factors.[31]

Table 2. Emission Integrated Intensity and PLQYs of $(C_{10}H_{16}N)_2Zn_{1-x}Mn_xBr_4$ (x = 0−1) under 450 nm Excitation

$(C_{10}H_{16}N)_2Zn_{1-x}Mn_xBr_4$	integrated intensity	PLQYs, %
x = 0	254.141	0
x = 0.01	4962.746	24.69
x = 0.05	34773.987	38.36
x = 0.10	58447.839	49.16
x = 0.15	75861.975	64.72
x = 0.2	92009.979	75.59
x = 0.4	112517.538	89.06
x = 0.6	116193.726	89.14
x = 0.8	119297.882	89.91
x = 1	120076.831	88.75

https://dx.doi.org/10.1021/acs.jpclett.0c01933
J. Phys. Chem. Lett. 2020, 11, 5956−5962

To experimentally certify the energy transfer of Mn^{2+}, the decay curves of $(C_{10}H_{16}N)_2Zn_{1-x}Mn_xBr_4$ (x = 0.2, 0.4, 0.6, 0.8, 1) are measured under 450 nm excitation. As illustrated in Figure 3d, the PL decay curves monitored at λ_{em} = 518 nm are well fitted by the single exponential decay equation:

$$I(t) = I_0 + A\exp(-t/\tau) \quad (1)$$

where $I(t)$ and I_0 are the luminescence intensity at time t and $t \gg \tau$, A is a constant, and τ is the decay time for an exponential component. The lifetimes of solid solutions are determined to be 0.33 ms, which is close to the literature values of Mn^{2+}-based bromides.[24] This further indicates that the green-light emission belongs to the d−d transition ($^4T_1$−$^6A_1$) of Mn^{2+}. Importantly, the lifetimes of $(C_{10}H_{16}N)_2Zn_{1-x}Mn_xBr_4$ (x = 0.2, 0.4, 0.6, 0.8, 1) do not change with the increase of Mn^{2+} concentration, which proves that there is quite weak energy transfer between adjacent luminescent centers of Mn^{2+}.

Following our past theoretical model describing the dependence of the luminescence intensity on the concentration of luminescent centers,[32] the luminescence intensity per unit volume of $(C_{10}H_{16}N)_2Zn_{1-x}Mn_xBr_4$ (x = 0−1) can be written as follows:

$$I_{em} = I_0 \cdot \frac{x \cdot A}{A + W_0 \cdot R^{-t}} \quad (2)$$

where I_0 is the luminescence intensity under the dilute condition; x is the content of Mn^{2+}, A is the spontaneous emission rate of the luminescent $^4T_1$ energy level of Mn^{2+}, t is the index of the Mn−Mn electric multipole interaction, W_0 is equal to the energy transfer rate of Mn^{2+} when R is unit length, and R is the Mn−Mn critical energy transfer distance, which also depends on the x with the Blasse formula:[33]

$$R = 2 \cdot \left(\frac{3V}{4\pi x n}\right)^{1/3} \quad (3)$$

where V is the unit cell volume and n is the number of Zn^{2+} sites in one unit cell. The brief derivation process of eq 2 was given in Supporting Information to understand the physical meaning of constant parameters. As shown in the inset of Figure 3c, the experimental Mn^{2+} concentration dependence of the emission intensity can be well fitted by the eq 2, indicating the important role of the Mn−Mn energy transfer on the luminescence intensity regulation. By taking eq 3 into eq 2, we have the direct numerical relationship of I_{em} versus x, as the values of I_0, A, W_0, and t can be determined by fitting the dependence of emission intensity of $(C_{10}H_{16}N)_2Zn_{1-x}Mn_xBr_4$ (x = 0−1) on the Mn^{2+} concentration. Table S2 summarizes the ratio of the energy transfer rate of Mn^{2+} to the spontaneous emission rate of the luminescent $^4T_1$ energy level of Mn^{2+}, i.e., $W_0 \cdot R^{-t}/A$, based on the application of the values obtained of W_0, A, and t. Obviously, the longer R, the smaller the energy transfer rate, and therefore much stronger luminescence intensity can be expected.

For those 0D Mn^{2+}-based metal halides, let us set x = 1 and substitute the optimized values of the fitting parameters into eq 2, and then the dependence of the emission intensity on the closest Mn−Mn distance can be predicted and shown in Figure 4. The calculated trend on R indicates that the longer R, the stronger emission intensity and thus the larger PLQY. Such an increasing trend can be explained as the weakening of the Mn−Mn energy transfer due to the increase manipulation of the closest Mn−Mn distance R, as shown by the inset of Figure 4.

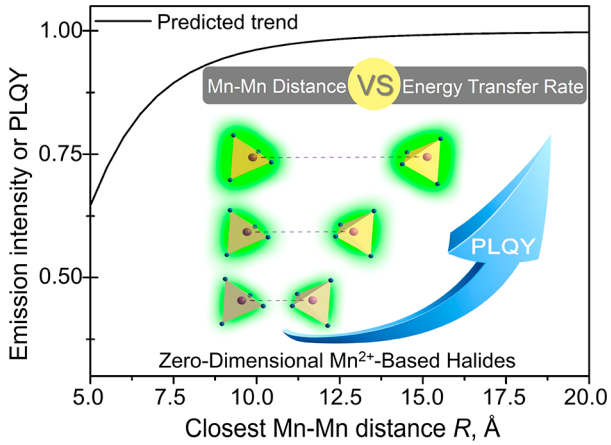

Figure 4. Predicted dependences of the emission intensity of Mn^{2+} on the closest Mn−Mn distance in 0D Mn^{2+}-based metal halides. The inset shows the model diagram.

In addition, it can be seen from our prediction that the luminescence saturation will happen when R > 15 Å. All the results presented here give a good echo to the observed increasing relationship between R and PLQY in Figure 1. Accordingly, the inset of Figure 4 also properly depicts a competitive relationship between the closest Mn−Mn distance and the energy transfer rate in 0D Mn^{2+}-based metal halides.

The electronic band structures and excitation energies of $(C_{10}H_{16}N)_2Zn_{1-x}Mn_xBr_4$ (x = 0, 1) were calculated with the HSE06 hybrid functional. As shown in Figure 5a,

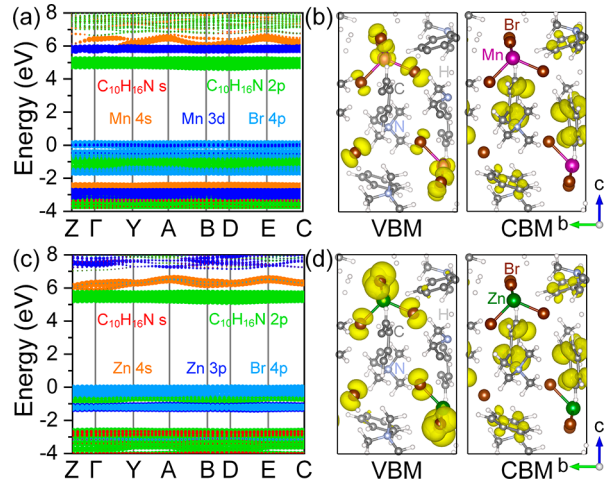

Figure 5. (a) Electronic band structures and (b) VBM- and CBM-associated charge densities of $(C_{10}H_{16}N)_2MnBr_4$. (c) Electronic band structures and (d) VBM- and CBM-associated charge densities of $(C_{10}H_{16}N)_2ZnBr_4$.

$(C_{10}H_{16}N)_2MnBr_4$ has a direct band gap of 4.60 eV at the D point, close to the experimental value of 4.55 eV (Figure S3b). The valence band maximum (VBM) consists of Br 4p and Mn 3d orbitals, while the conduction band minimum (CBM) is derived from the organic molecular $(C_{10}H_{16}N)$ 2p orbital. It can be found from Figure 5b that the contributions to VBM and CBM are concentrated on $MnBr_4$ clusters and organic groups, separately. The excitation energy was calculated to be 3.40 eV, close to the experimental value of 3.48 eV (Figure S3b). As shown in Figure 5c,d, $(C_{10}H_{16}N)_2ZnBr_4$ has a slightly indirect band gap of 5.14 eV, similar to the experimental value

https://dx.doi.org/10.1021/acs.jpclett.0c01933
J. Phys. Chem. Lett. 2020, 11, 5956−5962

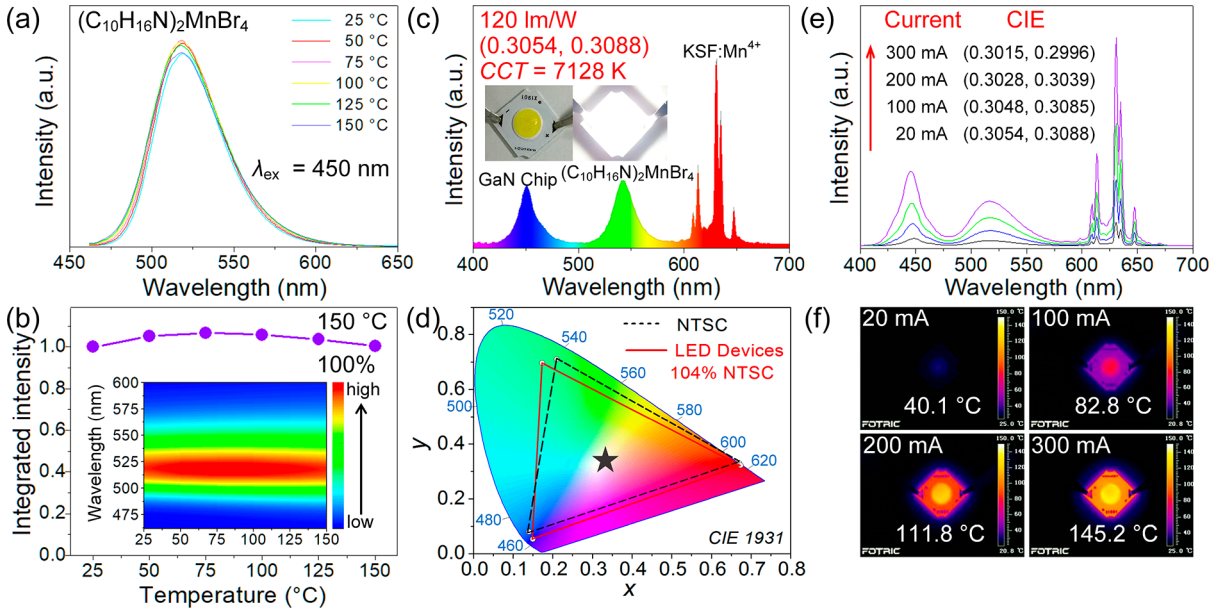

Figure 6. (a) Temperature-dependent PL spectra of $(C_{10}H_{16}N)_2MnBr_4$ under 450 nm excitation in the temperature range of room temperature to 150 °C with an interval of 25 °C. (b) Integrated PL intensity of $(C_{10}H_{16}N)_2MnBr_4$ as a function of temperature. The inset shows visual TQ behavior. (c) Emission spectrum of the white LED fabricated with the $(C_{10}H_{16}N)_2MnBr_4$ and the K_2SiF_6:Mn^{4+} on the InGaN chip (λ_{em} = 450 nm) at a 20 mA drive current. The insets show the photographs of device. (d) Color gamut of NTSC standard (black dotted line) and the fabricated white LED (red line, 104%) in the CIE 1931 system. (e) Drive current dependent emission spectra and CIE chromaticity coordinates of LED device. (f) Thermographs at different drive currents from 20 to 300 mA.

of 5.27 eV (Figure S3c). The VBM consisting of the Br 4p orbital is at the C point, and the CBM consisting of the $(C_{10}H_{16}N)$ 2p orbital is located at the D point. Note that the direct band gap at the D point is only 0.005 eV higher in energy. Unlike Mn^{2+} in $(C_{10}H_{16}N)_2MnBr_4$, Zn^{2+} has little contribution to the band edge of $(C_{10}H_{16}N)_2ZnBr_4$, due to the full d state (d^{10}). Besides, the excitation energy is calculated to be 4.96 eV, only slightly smaller the band gap value.

Temperature quenching (TQ) behaviors are regarded an important indicator of the potential of light-emitting materials for LED application. Initially, the thermogravimetric (TG) analysis (Figure S4) indicates $(C_{10}H_{16}N)_2MnBr_4$ is thermally stable up to around 215 °C, and the chemical stability of such hybrids is related to the organic ligands used here. As shown in Figure 6a and Figure S5, we also investigate the temperature-dependent PL spectra of $(C_{10}H_{16}N)_2Zn_{1-x}Mn_xBr_4$. As the temperature rises, no decline is observed for their integrated emission intensity. At 150 °C, the integrated emission intensity of solid solutions is about 100% of that at room temperature, indicating a zero-thermal PL quenching (Figure 6b). The isolated luminescence centers with lager Mn−Mn distance are key for such an excellent thermal stability, ascribed to the inhibition of energy migration with the increasing temperature. Moreover, $(C_{10}H_{16}N)_2MnBr_4$ exhibits a highly efficient narrow-band green emission (fwhm = 46 nm, λ_{em} = 518 nm, PLQY = 88.75%) under 450 nm excitation. Thus, the 0D Mn^{2+}-based metal halides may be attractive candidates as LED backlights for wide color gamut display. Accordingly, Figure 6c shows the white LED device fabricated by the green-emitting $(C_{10}H_{16}N)_2MnBr_4$, the red-emitting K_2SiF_6:Mn^{4+}, and a blue InGaN chip (λ_{em} = 450 nm), which exhibits a suitable correlated color temperature (CCT) of 7218 K, and a high luminous efficacy of 120 lm/W at a 20 mA drive current, and the CIE chromaticity coordinates of (0.3054, 0.3088) located on the white region. The as-fabricated white LED covers a wide color gamut of 104% NTSC in CIE 1931 (Figure 6d), suggesting its potential for LCDs backlighting. To further evaluate the thermal stability in industrial application, the drive current dependent emission spectra are measured at 20−300 mA (Figure 6e). The emission spectra are similar in shape with a small color shift. As shown in Figure 6f, the thermographs at different drive currents directly show the highest operating temperature (145.2 °C) of white LED device. That is to say that $(C_{10}H_{16}N)_2MnBr_4$ has no TQ behavior below 150 °C, which is attractive for use in the backlights of LCDs.

In summary, the solid solutions of $(C_{10}H_{16}N)_2Zn_{1-x}Mn_xBr_4$ (x = 0−1) were designed and synthesized to study the isolated $[MnBr_4]$ unit functionalization for inhibiting concentration quenching, and the new narrow-band green emitter with high PLQY was discovered via such a design principle. Remarkably, there is a competition between the closest Mn−Mn distance and the energy transfer rate of Mn^{2+}, and the unique 0D isolated structure casts a much longer Mn−Mn distance toward all luminescence centers of Mn^{2+} with spontaneous emission, which is a universal regulating strategy to achieve the highly efficient narrow-band green emission. As a typical case, $(C_{10}H_{16}N)_2MnBr_4$ exhibits a narrow-band green emission at 518 nm with a fwhm of 46 nm and an excellent thermal stability of zero-thermal quenching at 150 °C. The as-fabricated white LED device shows a high luminous efficacy of 120 lm/W and a wide color gamut of 104% NTSC, which can be used in the backlighting of LCDs. This work provides a versatile insight into the 0D Mn^{2+}-based metal halides with isolated $[MnBr_4]$ unit toward near-unity PL efficiency.

■ ASSOCIATED CONTENT

Supporting Information

The Supporting Information is available free of charge at https://pubs.acs.org/doi/10.1021/acs.jpclett.0c01933.

https://dx.doi.org/10.1021/acs.jpclett.0c01933
J. Phys. Chem. Lett. 2020, 11, 5956−5962

Experimental details, Rietveld refinement XRD patterns of $(C_{10}H_{16}N)_2Zn_{1-x}Mn_xBr_4$($x$ = 0−1) for Figure S1, PLE and PL spectra and the decay curve of $(C_{10}H_{16}N)_2ZnBr_4$ for Figure S2, diffuse reflectance spectra for Figure S3, TG curve of $(C_{10}H_{16}N)_2MnBr_4$ for Figure S4, temperature-dependent PL spectra for Figure S5, main parameters of processing and refinement for Tables S1, calculated values of the critical energy transfer distance (R) and the ratio of the energy transfer rate to the spontaneous emission rate for Table S2 (PDF)

Crystallographic data of $(C_{10}H_{16}N)_2ZnBr_4$ (CIF)

Crystallographic data of $(C_{10}H_{16}N)_2(Zn_{0.8}Mn_{0.2})Br_4$ (CIF)

Crystallographic data of $(C_{10}H_{16}N)_2(Zn_{0.6}Mn_{0.4})Br_4$ (CIF)

Crystallographic data of $(C_{10}H_{16}N)_2(Zn_{0.4}Mn_{0.6})Br_4$ (CIF)

Crystallographic data of $(C_{10}H_{16}N)_2(Zn_{0.2}Mn_{0.8})Br_4$ (CIF)

Crystallographic data of $(C_{10}H_{16}N)_2MnBr_4$ (CIF)

AUTHOR INFORMATION

Corresponding Authors

Zhiguo Xia − *The State Key Laboratory of Luminescent Materials and Devices, Guangdong Provincial Key Laboratory of Fiber Laser Materials and Applied Techniques, School of Materials Science and Technology, South China University of Technology, Guangzhou 510641, China; The Beijing Municipal Key Laboratory of New Energy Materials and Technologies, School of Materials Sciences and Engineering, University of Science and Technology Beijing, Beijing 100083, China;* orcid.org/0000-0002-9670-3223; Email: xiazg@scut.edu.cn

Chonggeng Ma − *CQUPT-BUL Innovation Institute, Chongqing University of Posts and Telecommunications, Chongqing 400065, China;* orcid.org/0000-0001-8090-1738; Email: cgma.ustc@gmail.com

Zewen Xiao − *Wuhan National Laboratory for Optoelectronics, Huazhong University of Science and Technology, Wuhan 430074, China;* orcid.org/0000-0002-4911-1399; Email: zwxiao@hust.edu.cn

Authors

Guojun Zhou − *The State Key Laboratory of Luminescent Materials and Devices, Guangdong Provincial Key Laboratory of Fiber Laser Materials and Applied Techniques, School of Materials Science and Technology, South China University of Technology, Guangzhou 510641, China; Key Laboratory of Magnetic Molecules and Magnetic Information Materials (Ministry of Education), School of Chemistry and Material Science, Shanxi Normal University, Linfen 041004, China; The Beijing Municipal Key Laboratory of New Energy Materials and Technologies, School of Materials Sciences and Engineering, University of Science and Technology Beijing, Beijing 100083, China*

Zhiyang Liu − *Wuhan National Laboratory for Optoelectronics, Huazhong University of Science and Technology, Wuhan 430074, China*

Jinglong Huang − *The State Key Laboratory of Luminescent Materials and Devices, Guangdong Provincial Key Laboratory of Fiber Laser Materials and Applied Techniques, School of Materials Science and Technology, South China University of Technology, Guangzhou 510641, China*

Maxim S. Molokeev − *Laboratory of Crystal Physics, Kirensky Institute of Physics, Federal Research Center KSC SB RAS, Krasnoyarsk 660036, Russia; Siberian Federal University, Krasnoyarsk 660041, Russia; Department of Physics, Far Eastern State Transport University, Khabarovsk 680021, Russia*

Complete contact information is available at: https://pubs.acs.org/10.1021/acs.jpclett.0c01933

Author Contributions

¶G.Z. and Z.L. contributed equally.

Notes

The authors declare no competing financial interest.

ACKNOWLEDGMENTS

This work was supported by the National Natural Science Foundations of China (Grant No. 51972118, 51961145101, and 51722202), Fundamental Research Funds for the Central Universities (D2190980), Guangzhou Science & Technology Project (202007020005), the Guangdong Provincial Science & Technology Project (No. 2018A050506004), and the Local Innovative and Research Teams Project of Guangdong Pearl River Talents Program (2017BT01X137). This work is also funded by RFBR according to the research project No. 19-52-80003. C. Ma acknowledges the support from the Innovation and Entrepreneurship Programs for Returned Overseas Chinese Scholars offered by Chongqing Bureau of Human Resources and Social Security (CX2019055). Z. Xiao acknowledges the financial support from the Thousand Young Talents Program of China, the Startup Fund of Huazhong University of Science and Technology, and the Director Fund of Wuhan National Laboratory for Optoelectronics.

REFERENCES

(1) Chen, H. W.; He, J.; Wu, S. T. Recent Advances on Quantum-Dot-Enhanced Liquid-Crystal Displays. *IEEE J. Sel. Top. Quantum Electron.* **2017**, *23*, 1−11.

(2) Protesescu, L.; Yakunin, S.; Bodnarchuk, M. I.; Krieg, F.; Caputo, R.; Hendon, C. H.; Yang, R. X.; Walsh, A.; Kovalenko, M. V. Nanocrystals of Cesium Lead Halide Perovskites ($CsPbX_3$, X = Cl, Br, and I): Novel Optoelectronic Materials Showing Bright Emission with Wide Color Gamut. *Nano Lett.* **2015**, *15*, 3692−3696.

(3) Liao, H. X.; Zhao, M.; Zhou, Y. Y.; Molokeev, M. S.; Liu, Q. L.; Zhang, Q. Y.; Xia, Z. G. Polyhedron Transformation toward Stable Narrow-Band Green Phosphors for Wide-Color-Gamut Liquid Crystal Display. *Adv. Funct. Mater.* **2019**, *29*, 1901988.

(4) Zhang, F.; Zhong, H. Z.; Chen, C.; Wu, X. G.; Hu, X.; Huang, H. L.; Han, J. B.; Zou, B. S.; Dong, Y. P. Brightly Luminescent and Color-Tunable Colloidal $CH_3NH_3PbX_3$ (X = Br, I, Cl) Quantum Dots: Potential Alternatives for Display Technology. *ACS Nano* **2015**, *9*, 4533−4542.

(5) Chen, H.-S.; Hsu, C.-K.; Hong, H.-Y. InGaN-CdSe-ZnSe Quantum Dots White LEDs. *IEEE Photonics Technol. Lett.* **2006**, *18*, 193−195.

(6) Quan, L. N.; Rand, B. P.; Friend, R. H.; Mhaisalkar, S. G.; Lee, T. W.; Sargent, E. H. Perovskites for Next-Generation Optical Sources. *Chem. Rev.* **2019**, *119*, 7444−7477.

(7) Li, S. X.; Xie, R.-J.; Takeda, T.; Hirosaki, N. Critical Review—Narrow-Band Nitride Phosphors for Wide Color-Gamut White LED Backlighting. *ECS J. Solid State Sci. Technol.* **2018**, *7*, R3064−R3078.

(8) Li, S. X.; Wang, L.; Tang, D. M.; Cho, Y. J.; Liu, X. J.; Zhou, X. T.; Lu, L.; Zhang, L.; Takeda, T.; Hirosaki, N.; Xie, R.-J. Achieving High Quantum Efficiency Narrow-Band β-Sialon:Eu^{2+} Phosphors for

https://dx.doi.org/10.1021/acs.jpclett.0c01933
J. Phys. Chem. Lett. 2020, 11, 5956−5962

High-Brightness LCD Backlights by Reducing the Eu^{3+} Luminescence Killer. *Chem. Mater.* **2018**, *30*, 494−505.
(9) Zhao, M.; Liao, H. X.; Ning, L. X.; Zhang, Q. Y.; Liu, Q. L.; Xia, Z. G. Next-Generation Narrow-Band Green-Emitting $RbLi(Li_3SiO_4)_2:Eu^{2+}$ Phosphor for Backlight Display Application. *Adv. Mater.* **2018**, *30*, 1802489.
(10) Duan, C. J.; Delsing, A. C. A.; Hintzen, H. T. Red Emission from Mn^{2+} on a Tetrahedral Site in $MgSiN_2$. *J. Lumin.* **2009**, *129*, 645−649.
(11) Zhou, G. J.; Jiang, X. X.; Molokeev, M.; Lin, Z. S.; Zhao, J.; Wang, J.; Xia, Z. G. Optically Modulated Ultra-Broad-Band Warm White Emission in Mn^{2+}-Doped $(C_6H_{18}N_2O_2)PbBr_4$ Hybrid Metal Halide Phosphor. *Chem. Mater.* **2019**, *31*, 5788−5795.
(12) Zhu, Y. L.; Liang, Y. J.; Liu, S. Q.; Li, H. R.; Chen, J. H. Narrow-Band Green-Emitting $Sr_2MgAl_{22}O_{36}:Mn^{2+}$ Phosphors with Superior Thermal Stability and Wide Color Gamut for Backlighting Display Applications. *Adv. Opt. Mater.* **2019**, *7*, 1801419.
(13) Zhang, S.; Liang, H.; Liu, Y.; Liu, Y.; Hou, D.; Zhang, G.; Shi, J. Y. Intensive Green Emission of $ZnAl_2O_4:Mn^{2+}$ under Vacuum Ultraviolet and Low-Voltage Cathode Ray Excitation. *Opt. Lett.* **2012**, *37*, 2511−2513.
(14) Song, E. H.; Zhou, Y. Y.; Wei, Y.; Han, X. X.; Tao, Z. R.; Qiu, R. L.; Xia, Z. G.; Zhang, Q. Y. A Thermally Stable Narrow-Band Green-Emitting Phosphor $MgAl_2O_4:Mn^{2+}$ for Wide Color Gamut Backlight Display Application. *J. Mater. Chem. C* **2019**, *7*, 8192−8198.
(15) Zhou, G. J.; Su, B. B.; Huang, J. L.; Zhang, Q. Y.; Xia, Z. G. Broad-Band Emission in Metal Halide Perovskites: Mechanism, Materials, and Applications. *Mater. Sci. Eng., R* **2020**, *141*, 100548.
(16) Zhou, C. K.; Lin, H. R.; Tian, Y.; Yuan, Z.; Clark, R.; Chen, B. H.; van de Burgt, L. J.; Wang, J. C.; Zhou, Y.; Hanson, K.; Meisner, Q. J.; Neu, J.; Besara, T.; Siegrist, T.; Lambers, E.; Djurovich, P.; Ma, B. W. Luminescent Zero-Dimensional Organic Metal Halide Hybrids with Near-Unity Quantum Efficiency. *Chem. Sci.* **2018**, *9*, 586−593.
(17) Zhang, Y.; Liao, W. Q.; Fu, D. W.; Ye, H. Y.; Chen, Z. N.; Xiong, R. G. Highly Efficient Red-Light Emission in an Organic-Inorganic Hybrid Ferroelectric: $(Pyrrolidinium)MnCl_3$. *J. Am. Chem. Soc.* **2015**, *137*, 4928−4931.
(18) Cai, X.-W.; Zhao, Y.-Y.; Li, H.; Huang, C.-P.; Zhou, Z. Lead-Free/Rare Earth-Free Green-Light-Emitting Crystal Based on Organic-Inorganic Hybrid $[(C_{10}H_{16}N)_2][MnBr_4]$ with High Emissive Quantum Yields and Large Crystal Size. *J. Mol. Struct.* **2018**, *1161*, 262−266.
(19) Jiang, C. L.; Zhong, N.; Luo, C. H.; Lin, H. C.; Zhang, Y. Y.; Peng, H.; Duan, C. G. $(Diisopropylammonium)_2MnBr_4$: A Multifunctional Ferroelectric with Efficient Green-Emission and Excellent Gas Sensing Properties. *Chem. Commun.* **2017**, *53*, 5954−5957.
(20) Xu, L.; Gao, J. X.; Chen, X. G.; Hua, X. N.; Liao, W. Q. A Temperature-Triggered Triplex Bistable Switch in a Hybrid Multifunctional Material: $[(CH_2)_4N(CH_2)_4]_2[MnBr_4]$. *Dalton Trans.* **2018**, *47*, 16995−17003.
(21) Xu, L. J.; Sun, C. Z.; Xiao, H.; Wu, Y.; Chen, Z. N. Green-Light-Emitting Diodes Based on Tetrabromide Manganese(II) Complex through Solution Process. *Adv. Mater.* **2017**, *29*, 1605739.
(22) Li, M. Z.; Zhou, J.; Molokeev, M. S.; Jiang, X. X.; Lin, Z. S.; Zhao, J.; Xia, Z. G. Lead-Free Hybrid Metal Halides with a Green-Emissive $[MnBr_4]$ Unit as a Selective Turn-On Fluorescent Sensor for Acetone. *Inorg. Chem.* **2019**, *58*, 13464−13470.
(23) Gong, L. K.; Hu, Q. Q.; Huang, F. Q.; Zhang, Z. Z.; Shen, N. N.; Hu, B.; Song, Y.; Wang, Z. P.; Du, K. Z.; Huang, X. Y. Efficient Modulation of Photoluminescence by Hydrogen Bonding Interactions between Inorganic $[MnBr_4]^{2-}$ Anions and Organic Cations. *Chem. Commun.* **2019**, *55*, 7303−7306.
(24) Morad, V.; Cherniukh, I.; Pöttschacher, L.; Shynkarenko, Y.; Yakunin, S.; Kovalenko, M. V. Manganese(II) in Tetrahedral Halide Environment: Factors Governing Bright Green Luminescence. *Chem. Mater.* **2019**, *31*, 10161−10169.
(25) Su, B. B.; Molokeev, M. S.; Xia, Z. G. Mn^{2+}-Based Narrow-Band Green-Emitting Cs_3MnBr_5 Phosphor and The Performance Optimization by Zn^{2+} Alloying. *J. Mater. Chem. C* **2019**, *7*, 11220−11226.
(26) Shannon, R. D. Revised Effective Ionic Radii and Systematic Studies of Interatomic Distances in Halides and Chalcogenides. *Acta Crystallogr., Sect. A: Cryst. Phys., Diffr., Theor. Gen. Crystallogr.* **1976**, *32*, 751−767.
(27) Smith, M. D.; Karunadasa, H. I. White-Light Emission from Layered Halide Perovskites. *Acc. Chem. Res.* **2018**, *51*, 619−627.
(28) Zhou, G. J.; Li, M. Z.; Zhao, J.; Molokeev, M. S.; Xia, Z. G. Single-Component White-Light Emission in 2D Hybrid Perovskites with Hybridized Halogen Atoms. *Adv. Opt. Mater.* **2019**, *7*, 1901335.
(29) Zeng, H. B.; Duan, G. T.; Li, Y.; Yang, S. K.; Xu, X. X.; Cai, W. P. Blue Luminescence of ZnO Nanoparticles Based on Non-Equilibrium Processes: Defect Origins and Emission Controls. *Adv. Funct. Mater.* **2010**, *20*, 561−572.
(30) Panigrahy, B.; Aslam, M.; Misra, D. S.; Ghosh, M.; Bahadur, D. Defect-Related Emissions and Magnetization Properties of ZnO Nanorods. *Adv. Funct. Mater.* **2010**, *20*, 1161−1165.
(31) Dexter, D. L.; Schulman, J. H. Theory of Concentration Quenching in Inorganic Phosphors. *J. Chem. Phys.* **1954**, *22*, 1063−1070.
(32) Zhang, Z. C.; Ma, C. G.; Gautier, R.; Molokeev, M. S.; Liu, Q. l.; Xia, Z. G. Structural Confinement toward Giant Enhancement of Red Emission in Mn^{2+}-Based Phosphors. *Adv. Funct. Mater.* **2018**, *28*, 1804150.
(33) Blasse, G. Energy Transfer in Oxidic Phosphors. *Phys. Lett. A* **1968**, *28*, 444−445.

https://dx.doi.org/10.1021/acs.jpclett.0c01933
J. Phys. Chem. Lett. 2020, 11, 5956−5962